**Key Points:**
- We model magma transport beneath a mid-ocean ridge with variable grain-size and non-Newtonian viscosity
- Models show melt focusing by a previously unrecognized mechanism based on compaction pressure gradients from melting rate and viscosity
- Grain-size and non-Newtonian viscosity are properties of the solid but their effect on magmatic flow is more profound than on solid flow

**Correspondence to:**
R. F. Katz,
richard.katz@earth.ox.ac.uk

# Magmatic Focusing to Mid-Ocean Ridges: The Role of Grain-Size Variability and Non-Newtonian Viscosity

Andrew J. Turner[1] [ID], Richard F. Katz[1] [ID], Mark D. Behn[2] [ID], and Tobias Keller[3] [ID]

[1]Department of Earth Sciences, University of Oxford, Oxford, UK, [2]Department of Geology and Geophysics, Woods Hole Oceanographic Institution, Woods Hole, MA, USA, [3]Department of Geophysics, Stanford University, Stanford, CA, USA

**Abstract** Melting beneath mid-ocean ridges occurs over a region that is much broader than the zone of magmatic emplacement that forms the oceanic crust. Magma is focused into this zone by lateral transport. This focusing has typically been explained by dynamic pressure gradients associated with corner flow, or by a sublithospheric channel sloping upward toward the ridge axis. Here we discuss a novel mechanism for magmatic focusing: lateral transport driven by gradients in compaction pressure within the asthenosphere. These gradients arise from the covariation of melting rate and compaction viscosity. The compaction viscosity, in previous models, was given as a function of melt fraction and temperature. In contrast, we show that the viscosity variations relevant to melt focusing arise from grain-size variability and non-Newtonian creep. The asthenospheric distribution of melt fraction predicted by our models provides an improved explanation of the electrical resistivity structure beneath one location on the East Pacific Rise. More generally, we find that although grain-size and non-Newtonian viscosity are properties of the solid phase, their effect on melt transport beneath mid-ocean ridges is more profound than their effect on the mantle corner flow.

## 1. Introduction

Melting beneath mid-ocean ridges occurs over a broad region of order 100 km width in the plate-spreading direction (Forsyth et al., 1998). By contrast, magmatic emplacement to form the oceanic crust is limited to a zone that is ∼5 km in width, centered on the ridge axis (Carbotte et al., 2015). Magmatic focusing refers to the process or processes by which magma is extracted from the broad source region and transported to the narrow emplacement zone. The mechanism, lateral extent, and efficiency of magmatic focusing have been a subject of considerable interest in theoretical models of mid-ocean ridge magmatism (see review by Kelemen et al. (1997)).

There are two dominant hypotheses for magmatic focusing in that literature. The first argues that the dynamic pressure gradient arising from plate-driven, asthenospheric corner flow sucks melt laterally toward the ridge axis (Phipps Morgan, 1987; Spiegelman & McKenzie, 1987). The second argues that crystallization at the base of the thermal lithosphere creates an impermeable layer sloping upward toward the ridge axis; magma is then channelized along this barrier toward the ridge axis (Hebert & Montési, 2010; Sparks & Parmentier, 1991; Spiegelman, 1993b). This latter mechanism has been used to model melt focusing in 3-D along specific ridge systems (e.g., Magde & Sparks, 1997; Montési et al., 2011) and oceanic transform faults (Bai & Montési, 2015; Gregg et al., 2009). Keller et al. (2017) describe two-phase flow models indicating that both mechanisms contribute to focusing. However, it is unclear whether either corner flow suction or the sublithospheric-permeability-barrier mechanism are supported by observations. To focus melt over distances of ∼60 km, the former requires asthenospheric viscosities (∼$10^{21}$ Pa s) that are unrealistically high, based on laboratory estimates (Hirth & Kohlstedt, 2003). The latter predicts a high-porosity layer (melt volume fractions of several percent) beneath the lithosphere that should be detectable by seismic or magnetotelluric (MT) methods, but to date has not been detected in the vicinity of a mid-ocean ridge. Indeed, a recent magnetotelluric inversion of electrical resistivity beneath the northern East Pacific Rise suggests a style of magmatic flow that has not been predicted by any models of melt focusing at mid-ocean ridges (Key et al., 2013).

Key et al. (2013) image a triangular region of diminished resistivity between about 10 and 100 km depth beneath the ridge axis (their results are shown in our summary, Figure 4). The sides of this region are

relatively sharp and dip at about 45° away from the ridge axis. Assuming that this resistivity structure is broadly representative of the volume fraction of silicate melts, this observation is inconsistent with the sublithospheric-permeability-barrier mechanism for melt focusing: there is no evidence for an off-axis, low-resistivity layer at depths immediately beneath the thermal lithosphere. Rather, there is a high-resistivity region that extends off-axis from ∼5 km depth to the sides of the low-resistivity triangle. Previous focusing hypotheses (Sparks & Parmentier, 1991; Spiegelman & McKenzie, 1987) and more recent computational models (Ghods & Arkani-Hamed, 2000; Katz, 2008; Keller et al., 2017) predict nonzero or even upward-increasing melt fraction in these regions, which should be associated with modest to low resistivity (Miller et al., 2015).

These observations motivate a re-examination of the mechanisms by which melt is focused beneath mid-ocean ridges. Permeability, which is a key control on melt segregation, is highly sensitive to grain size (Miller et al., 2014; von Bargen & Waff, 1986). As such, several studies have analyzed the effects of grain-size variability on magmatic focusing in subduction zones (Cagnioncle et al., 2007; Cerpa et al., 2017; Wada & Behn, 2015; Wada et al., 2011). For mid-ocean ridges, Turner et al. (2015) coupled single-phase, passive mantle flow with composite, non-Newtonian viscosity, and grain-size evolution. Steady state solutions predicted an upward decrease in grain size within an elongated zone that slopes toward the ridge axis. Although the model by Turner et al. (2015) did not include an explicit prediction of magmatic flow, the layer of small grain size was interpreted as a barrier to vertical magmatic segregation (albeit a leaky one). Intriguingly, this layer is coincident with the margin of the low-resistivity region in the Key et al. (2013) MT observations. This led Turner et al. (2015) to hypothesize that grain size plays an important role in focusing magma toward the axis at mid-ocean ridges.

In the present paper, we develop two-phase flow models of magma/mantle interaction in a variable grain-size mantle to investigate the focusing hypothesis of Turner et al. (2015). Our models compute the mean grain-size field as in that work, but further couple it with conservation of mass, momentum, and energy for a liquid phase (the magma) and a solid phase (the mantle) (Keller & Katz, 2016; McKenzie, 1984). We obtain a pattern of magmatic segregation that exhibits strong focusing toward the ridge axis. However, the focusing mechanism is more complex than envisioned by Turner et al. (2015) and cannot be explained by the spatial structure of permeability that arises from the grain-size field. Rather, focusing is linked to variations in melting rate and asthenospheric viscosity, which is in turn linked to grain size, but through its influence on viscosity. The resulting focusing mechanism is previously unrecognized and predicts melt distributions beneath the ridge axis that are broadly consistent with the resistivity structure of Key et al. (2013). Below we present our numerical two-phase results after a brief exposition of the theory and methods used in this study. These results are followed by a discussion of the causative physical mechanisms for melt focusing.

## 2. Methods

The overall method used in this work is computational modeling of geodynamic processes by solution of partial differential equations. In this section, we describe the physical processes that are incorporated in the governing equations and the assumptions that are used to simplify those equations. We provide a brief overview of the numerical methods used to discretize and solve the system.

### 2.1. Mechanics and Thermochemistry

The two-phase model comprises statements of conservation of mass and momentum for a liquid ($\ell$) and a solid ($s$) phase. The volume fraction of liquid within a representative volume element is $\phi(\mathbf{x}, t)$. The density of each phase is considered constant and the two densities are considered equal (to $\rho$) except in terms representing the body force, where the solid-minus-liquid difference is denoted $\Delta\rho$ (the extended Boussinesq approximation). Following McKenzie (1984),

$$\nabla \cdot \overline{\mathbf{v}} = 0, \tag{1a}$$

$$\frac{\partial \phi}{\partial t} - \nabla \cdot (1-\phi)\mathbf{v}_s = \Gamma/\rho, \tag{1b}$$

$$\nabla P - \nabla \cdot 2\eta\dot{\varepsilon} - \nabla(\zeta_\phi - 2\eta/3)\nabla \cdot \mathbf{v}_s = -\phi\Delta\rho\mathbf{g}, \tag{1c}$$

$$\nabla P + K_\phi^{-1}\phi(\boldsymbol{v}_\ell - \boldsymbol{v}_s) = -\Delta\rho\boldsymbol{g}. \tag{1d}$$

The first equation, in which $\overline{\boldsymbol{v}} = \phi\boldsymbol{v}_\ell + (1-\phi)\boldsymbol{v}_s$, is a continuity equation that expresses conservation of mass for the bulk, two-phase system. The second equation represents conservation of mass for the solid phase; $\Gamma$ is the melting rate in mass/volume/time. The third equation represents Stokesian momentum conservation for the aggregate; $\nabla P \equiv \nabla P_\ell - \rho\boldsymbol{g}$ is a dynamic pressure gradient; $\dot{\varepsilon} \equiv \frac{1}{2}\left[\nabla\boldsymbol{v}_s + (\nabla\boldsymbol{v}_s)^T\right]$ is the strain rate tensor; $\eta$ and $\zeta_\phi$ are the shear and compaction viscosity, respectively, and $\boldsymbol{g}$ is the acceleration of gravity. The fourth equation represents Darcian momentum conservation in the liquid phase; $K_\phi \equiv k_\phi/\mu$ is the ratio of permeability to magma viscosity.

The general characteristics and behavior of this system of equations are discussed in the literature (e.g., McKenzie, 1984; Rudge, 2014; Scott & Stevenson, 1986; Spiegelman, 1993b). Of particular interest here is the Darcian segregation flux, $\boldsymbol{q} \equiv \phi(\boldsymbol{v}_\ell - \boldsymbol{v}_s)$, which is driven by dynamic pressure gradients and magma buoyancy associated with the interphase density difference, according to equation (1d).

This system of equations is closed by equations for the melting rate $\Gamma$, the liquid mobility $K_\phi$, and the aggregate shear $\eta$ and compaction $\zeta_\phi$ viscosities. The melting rate is computed by coupling the mechanical system (1) with a thermochemical system that represents conservation of energy and species mass, and with a kinetic formulation for melting reactions called R_DMC (see Keller & Katz, 2016, for details). We use a two-pseudocomponent system, where the pseudocomponents are the product (a fertile basalt) and residual (a refractory harzburgite) of MORB-type mantle melting (Ribe, 1985; Shorttle et al., 2014). The system is calibrated such that upwelling mantle begins melting at ∼65 km depth, and attains a degree of melting and crustal thickness that are consistent with observations (e.g., White et al., 2001).

## 2.2. Constitutive Laws

The permeability of the solid aggregate is parameterized on empirical and theoretical grounds as $k_\phi = a^2\phi^r/b$, where $a$ is the mean grain size; $r$ and $b$ are empirical constants, taken as 2 and 500 here (Miller et al., 2014, and references therein). This is valid at porosities below the disaggregation threshold of about 0.3.

The viscosity of the aggregate is treated by Turner et al. (2015) as a harmonic mean of flow laws for diffusion creep, dislocation creep, and dislocation-accommodated grain-boundary sliding (GBS). All of these creep processes are thermally activated, but only dislocation creep and GBS are non-Newtonian, and only diffusion creep and GBS are grain-size sensitive. Here we adopt a single shear-viscosity law that is sufficiently general to incorporate all of these dependencies

$$\eta = \eta_0\langle a\rangle^{m/n}\langle\dot{\varepsilon}_{II}\rangle^{(1-n)/n}\exp\left[\frac{E/n}{RT_0}\left(\frac{1}{\langle T\rangle} - 1\right)\right], \tag{2}$$

where $\dot{\varepsilon}_{II}$ is the second invariant of the strain rate tensor, $m$ and $n$ are constants, $E$ is the activation energy, $R$ is the universal gas constant, and $T$ is the temperature. Quantities in angular brackets are normalized by a reference value, e.g., $\langle a\rangle = a/a_0$. Variations in shear viscosity with melt fraction are neglected because for small $\phi$, they are smaller than other variations. See Table 1 for parameter and reference values. We note that some studies have simplified this formulation by combining the $m/n$ dependence into a single $m$ coefficient (e.g., Rozel et al., 2011); however, for clarity, we retain the explicit form of the equation even though many of the individual parameters are not constrained precisely.

We eschew the well-established use of a composite viscosity for two reasons. First, model development in this work couples together physics that, in the context of two-phase flow, has not previously been

**Table 1**
*Meanings, Values, and Units for Symbols Used in this Paper*

| Quantity | Description | Value | Units |
|---|---|---|---|
| $a$ | Grain size | 0.003 or calculated | m |
| $a_0$ | Reference grain size | 0.01 | m |
| $\dot{\varepsilon}_{II}$ | Second invariant of strain rate | Calculated | $s^{-1}$ |
| $\dot{\varepsilon}_{II,0}$ | Reference second invariant of strain rate | $2.5 \times 10^{-14}$ | $s^{-1}$ |
| $E/n$ | Activation energy | $4.4 \times 10^5$ | J mol$^{-1}$ |
| $T$ | Temperature | Calculated | K |
| $T_0$ | Reference temperature | 1,623 | K |
| $\eta_0$ | Reference shear viscosity | $5 \times 10^{18}$ | Pa s |
| $R_\zeta$ | Bulk viscosity constant | 15 | |
| $r$ | Permeability melt fraction exponent | 2 | |
| $b$ | Permeability constant | 500 | |
| $p$ | Grain growth exponent | 5 | |
| $m$ | Grain rheology exponent | See text | |
| $n$ | Stress exponent | See text | |
| $K_g$ | Grain growth constant | $6.67 \times 10^{-11}$ | $m^5 s^{-1}$ |
| $E_g$ | Grain growth activation energy | $3.35 \times 10^5$ | J mol$^{-1}$ |
| $\psi$ | Recrystallization-rate lumped prefactor | 0.0625 | $m^2 J^{-1}$ |
| $\rho$ | Density (Boussinesq) | 3,200 | kg m$^{-3}$ |
| $\Delta\rho$ | Density difference (Boussinesq) | 500 | kg m$^{-3}$ |
| $\phi$ | Melt fraction | Calculated | |
| $\Gamma$ | Melting rate | Calculated | kg m$^{-3}$ s$^{-1}$ |
| $\mu$ | Liquid viscosity | 10 | Pa s |
| $\boldsymbol{v}_s$ | Solid velocity | Calculated | m s$^{-1}$ |
| $\boldsymbol{v}_\ell$ | Fluid velocity | Calculated | m s$^{-1}$ |
| $\boldsymbol{q}$ | Separation flux | Calculated | m s$^{-1}$ |

*Note.* Parameters not listed here are as given in Table 1 of Keller and Katz (2016). The activation energy $E_g$ is based on Hirth and Kohlstedt (1995), Hirth and Kohlstedt (2003), and Nichols and Mackwell (1991). The prefactor $K_g$ is consistent with Turner et al. (2015) after adjusting for a different grain growth exponent and activation energy.

studied. The associated parameter space and range of solution behavior is large and thus a systematic understanding requires the detailed parameter study below. A composite viscosity with a poorly constrained balance between mechanisms would complicate this study: if the assumed balance of mechanisms is incorrect, the parameter study would not reveal the relevant model behavior. The present approach clearly exposes the predicted physical control of parametric variations.

An application of this insight to the natural system is not straightforward, however, and this is related to the second reason for using equation (2). The interplay between grain size and viscosity in the mantle is complicated by factors including polydispersivity of grain size, coexistence of multiple mineral phases with different properties, crystal anisotropy, and mutual grain-size pinning—the rheological consequences of which have been little studied (though see Hansen & Warren, 2015; Tasaka et al., 2013, 2014; Tasaka & Hiraga, 2013). Hence, while the broad systematics of our coupled viscosity and grain-size model of the mantle should be reasonable, it would be a mistake to assume it (or any related formulation) is accurate. In this context, simplification of the viscosity formulation is judicious.

The compaction viscosity is simply related to the shear viscosity according to

$$\zeta_\phi = R_\zeta \frac{\eta}{\phi},\tag{3}$$

where $R_\zeta$ is a dimensionless constant with a value between 1 and 20 (Simpson et al., 2010a, 2010b; Takei & Holtzman, 2009).

### 2.3. Grain-Size Dynamics

The permeability and the shear viscosity have an explicit dependence on grain size, which is fundamental to the focusing hypothesis of Turner et al. (2015). Hence, we follow Turner et al. (2015) in incorporating a model of variations in the mean grain size based on the Wattmeter formulation of Austin and Evans (2007, 2009). We give a brief review of the model and refer the reader to Turner et al. (2015) and Behn et al. (2009) for details.

The mean grain size varies according to

$$\frac{\partial a}{\partial t} + \mathbf{v}_s \cdot \nabla a = \frac{K_g}{p} a^{1-p} \exp\left[-E_g/(RT)\right] - \psi a^2 \eta \dot{\varepsilon} : \dot{\varepsilon}.\tag{4}$$

This equation states that grain-size variation along mantle flow lines is due to independent processes of growth by material diffusion between grains and reduction by recrystallization. $K_g$ and $E_g$ are the grain growth prefactor and activation energy, respectively. $p$ is an exponent that, for an unpinned, single-phase polycrystalline aggregate is in the range 2–3 (Atkinson, 1988; Burke & Turnbull, 1952; Hillert, 1965). Experiments suggest, however, that in the presence of a minor, pinning phase, the grain growth exponent should be taken as 4–6 or even greater (Hiraga et al., 2010; Tasaka & Hiraga, 2013; Thielmann et al., 2015). We adopt the value of $p = 5$ here.

The second term on the right-hand side of equation (4) represents grain-size reduction by conversion of the rate of viscous work into the formation rate of new grain boundaries. $\psi$ is a lumped prefactor that scales this rate. In models that employ a composite viscosity formulation, $\psi$ varies in proportion to the fraction of deformational work that is achieved locally by dislocation-based creep mechanisms (e.g., Turner et al., 2015). Furthermore, Rozel et al. (2011) found that it may be temperature dependent. For simplicity, here we follow Austin and Evans (2007, 2009) and force $\psi$ to be constant. Its value is chosen to give a mean grain size consistent with the current consensus in the literature. It is within a factor of 2 of the value used by Austin and Evans (2007), under the assumption that deformation is dominated by dislocation creep. However, De Bresser et al. (1998, 2000) showed that the coupled dynamics may drive the system toward equipartitioning of strain rate between diffusion and dislocation mechanisms, with an associated balance between grain growth and recrystallization. The viscosity in this balanced state might be reasonably represented with a noncomposite flow law such as (2), though the appropriate parameter values remain uncertain. See Turner et al. (2015) for a discussion of the parametric sensitivity of the grain-size distribution.

### 2.4. Boundary Conditions and Numerical Methods

The model is formulated as equations (1) and (4) with constitutive laws (2) and (3), and with the thermochemical model of Keller and Katz (2016). The body force in the aggregate force balance equation (1c) is of

order $\phi$ and hence we neglect it for simplicity. The domain is two-dimensional, rectangular, and aligned vertically and with the spreading direction. One lateral edge is directly beneath the mid-ocean ridge axis and is assumed to be a line of bilateral symmetry. The top boundary represents the surface of the oceanic crust and has an imposed velocity of $\boldsymbol{v}_s(z=0)=(4\,\text{cm/yr})\hat{\boldsymbol{x}}\tanh(2x/x_r)$, where $x_r$ is the width of distributed extension by normal faulting at the ridge axis. On the bottom (inflow) and side (outflow) boundaries, the normal derivative of the normal stress is zero. The temperature on the top boundary is set to zero Celsius, while the mantle potential temperature (on the bottom boundary) is set to 1,350°C. Grain size has an imposed value of 3 mm on the bottom boundary. The fertile component is assumed to comprise 20% of the homogeneous, unmelted mantle source. Magma is allowed to leave the domain at the ridge axis by enforcing no melting or freezing within a region of width $x_r$ beneath the ridge axis. Over this width, the pressure on the top boundary is set to enforce zero normal gradient in the Darcy segregation flux.

The governing equations are discretized by finite volume and finite difference methods on a staggered grid (Katz et al., 2007; Keller & Katz, 2016) of model dimensions 400 km wide × 250 km deep with a grid resolution of 0.75 km. Time-stepping is semi-implicit and time step size is computed adaptively according to the magnitude of the maximum liquid velocity over the domain. The system of discrete equations is solved at each time step with an outer iteration in which the mechanics, the thermochemistry, and the grain-size solutions are each updated separately. This iteration is halted when a specified tolerance for the fully coupled residual is achieved or after five cycles have been completed. The mechanical solution is obtained using the sparse direct solver MUMPS (Amestoy et al., 2001), while the other equations are solved using block-Jacobi preconditioned GMRES. The data structures and parallel methods are provided by the Portable Extensible Toolkit for Scientific Computation (Balay et al., 2016a, 2016b).

## 3. Results of End-Member Models

The theory described above is used to calculate grain-size evolution and two-phase flow in two end-member cases. The first case is a *base model* with Newtonian rheology and spatially uniform grain size. In the second, the *full model*, we solve for a fully coupled system with non-Newtonian rheology and dynamic grain-size evolution. Below we summarize the results of both sets of simulations and their predictions for melt migration beneath the ridge axis.

### 3.1. Newtonian; Constant Grain Size (Base Model)

The base model is constructed by imposing a static and spatially uniform grain size of 3 mm. Mantle rheology is constrained to be Newtonian ($n=1$) and grain-size insensitive ($m=0$). In this case, the shear viscosity and permeability are solely functions of the temperature and melt fraction, respectively. This model setup is similar to that originally proposed by Sparks and Parmentier (1991) and calculated numerically by Katz (2010).

Melt migration in the base model is subvertical throughout much of the melting region (Figure 1a). Immediately below the lithospheric thermal boundary layer, melt is deflected toward the ridge axis in a narrow zone, ~5 km wide. Melt fractions in the mantle are generally low ($\leq$1%), increasing gradually upward and toward the ridge axis. The location of the zone in which melt flow is deflected horizontally is determined by the balance between the compaction rate, the rate of melt supply from below, and crystallization from above (Spiegelman, 1993b). The depth at which the crystallization rate exceeds the melt supply closely follows the 1,250°C isotherm (Figure 1b). The deflection of melt along this boundary results from the vertical gradient in compaction pressure (Figure 1h), which produces a net force that retards the upward, buoyancy-driven transport of melt and deflects it laterally toward the ridge axis.

This result is consistent with the decompaction channel model originally proposed by Sparks and Parmentier (1991); however, our calculations predict lower melt fractions in the channel. Two possible reasons for this discrepancy are, first, a longer compaction length in our models and, second, that our boundary condition for melt extraction at the ridge axis adds an additional component of suction toward the ridge.

Toward the margins of the melting region, solitary waves are observed to arrive along the base of thermal boundary layer. These features are suppressed near the ridge axis due to the higher melting rates (Figure 1b) associated with enhanced mantle upwelling directly beneath the axis (Spiegelman, 1993a). On the limbs
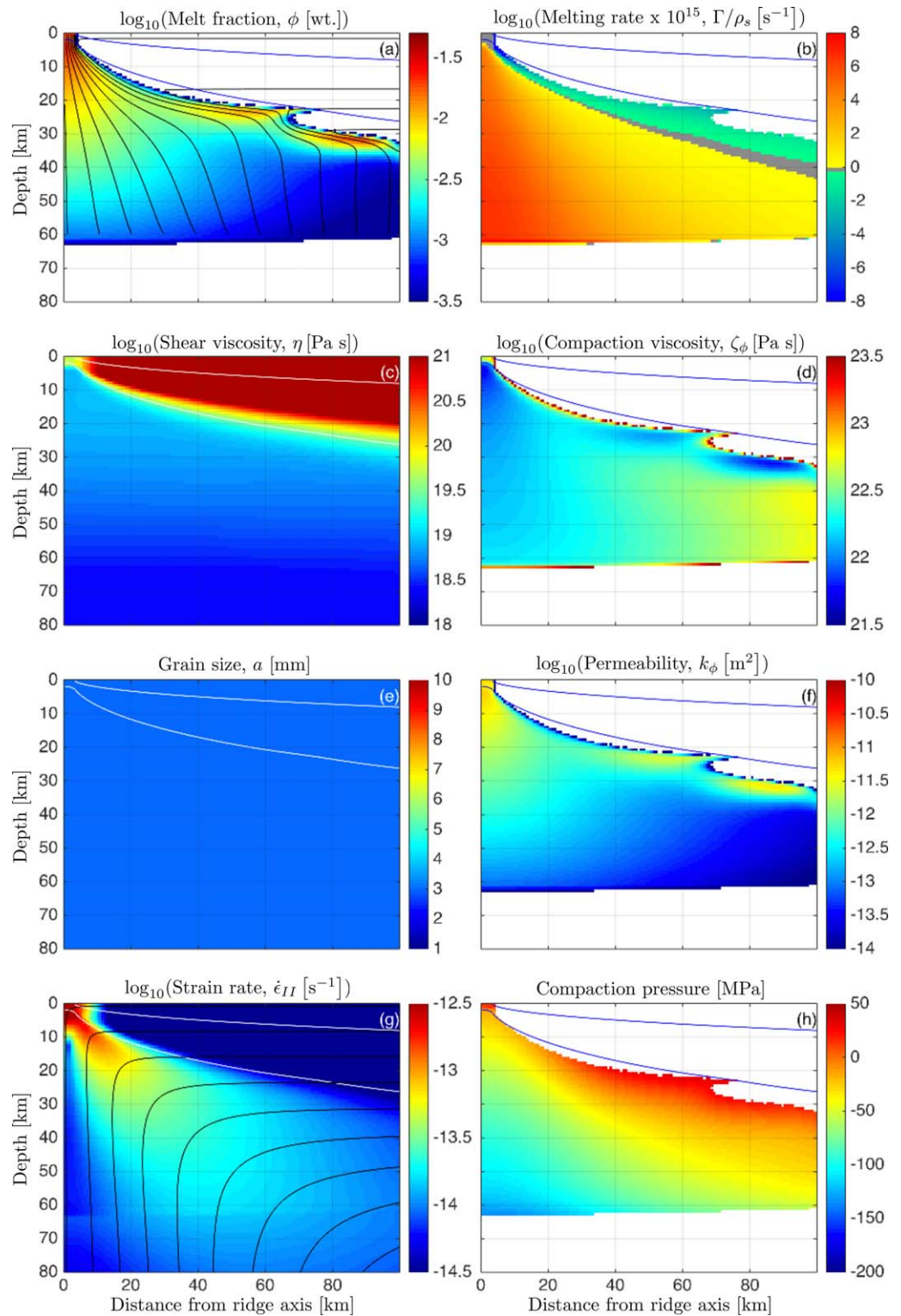
**Figure 1.** The base model run to a steady state (except for the compaction waves at the distal end of the melting region). The viscosity is Newtonian (equation (2)) with $n = 1$ and $m = 0$. Each plot shows isotherms at 600°C and 1,250°C as either white or blue lines. (a) Base-10 logarithm of melt fraction $\phi$ with streamlines of the magma flow field $v_\ell$ (black) superimposed. (b) Volumetric volume production rate of magma in inverse seconds, scaled by $10^{15}$. (c) Base-10 logarithm of shear viscosity $\eta$. (d) Base-10 logarithm of compaction viscosity $\zeta_\phi$. (e) Grain size in millimeters (constant and uniform, in this case). (f) Base-10 logarithm of permeability in $m^2$. (g) Base-10 logarithm of the second invariant of the strain rate tensor with streamlines of the mantle flow field $v_s$ (black) superimposed. (h) Compaction pressure. Positive values indicate liquid overpressure with respect to the solid.

of the partially molten region, however, the melting rate is insufficient to suppress the formation of solitary waves, leading to a time-dependence in the solutions, but only at distances $\gtrsim$50 km from the ridge axis.

### 3.2. Non-Newtonian; Variable Grain Size (Full Model)

We next consider the full model, shown in Figure 2, in which grain-size evolution is coupled to the mantle deformation field. Mantle viscosity is non-Newtonian with a stress exponent ($n = 3.5$) and grain-size sensitivity ($m = 2$). The resulting grain-size field is characterized by relatively large grain sizes directly beneath the ridge axis and within the lower lithosphere (Figure 2e). Grain sizes are smallest near the surface and within a portion of the melting region that extends downward from the ridge axis at an angle of 45°. This grain-size distribution is consistent with earlier single-phase simulations that did not incorporate melt migration (Turner et al., 2015). The dipping layer of reduced grain size is the result of high strain rates caused by the corner flow; it corresponds to a region of low permeability (Figure 2f) that is not observed in the base model (Figure 1f). However, the variability in permeability more closely mirrors the porosity (Figure 2a). Establishing causality, in this context, appears to be a "chicken/egg" problem, but an analysis in the next section clarifies the minimal importance of the permeability in the overall dynamics.

The distribution of melt beneath the axis (Figure 2a) is dramatically different in the full model as compared to the base model. Specifically, melt is concentrated in a relatively narrow region ($\sim$20 km wide) directly beneath the ridge axis, while the melt fraction in the off-axis mantle decreases relative to the base model. These variations in melt fraction correspond to changes in the trajectories of melt transport. In the fully coupled model, melt flow is directed vertically beneath the ridge axis, where melt fractions are highest. However, at distances $\gtrsim$10 km from the ridge, melt flow is sharply deflected toward the axis and follows horizontal trajectories. Indeed, at distances $\sim$20–40 km from the axis, melts are predicted to travel slightly downward as they approach the ridge axis (Figure 2a; discussed in the next section). In the same model, a small zone of high melt fraction is observed 40–70 km off-axis at the base of the thermal boundary layer. Although this is not part of a continuous, high-porosity channel extending to the ridge axis, it does host freezing and decompaction; hence, it can be considered a segmented decompaction channel that coexists with the deeper focusing mechanism.

## 4. Model Sensitivity

The full model end-member shown in Figure 2 illustrates a striking difference in melt transport from the canonical view associated with the base model, which has Newtonian viscosity and constant grain size (Figure 1). These two calculations differ in several ways: the permeability and the viscosity structure associated with grain-size variation, as well as the viscosity structure associated with the strain rate dependence. Turner et al. (2015) considered that only the permeability structure would modify melt segregation, but from the end-member models, it is impossible to disentangle the contributions of these different factors. Below we present a parameter study to help clarify the key physics controlling these differences.

To highlight and analyze the role of each factor, we focus attention on the subdomain at lateral distances of 20 and 40 km from the ridge axis at depths less than 60 km. There, the segregation of melt in the full model is dominantly lateral (Figure 2a), indicating that buoyancy is not the primary driver of segregation. In fact there is a region, enclosed by a dashed line, in which the segregation flux $\boldsymbol{q} \cdot \hat{\boldsymbol{z}} \leq 0$, meaning that the vertical component of the liquid velocity is less than that of the solid, though it may still be positive. Within that region, there is a smaller region in which $(\boldsymbol{v}_\ell + \boldsymbol{v}_s) \cdot \hat{\boldsymbol{z}} \leq 0$, which means that melt is driven downward, against buoyancy. Downward melt flow was also obtained by Spiegelman and McKenzie (1987), though in that case it was driven by the large dynamic pressure gradients of corner flow with unrealistically high shear viscosity. Under these conditions, where buoyancy is balanced by a vertical pressure gradient, lateral melt transport can become dominant. Hence, the problem of understanding focusing can be approximately reduced to understanding the vertical pressure gradient that balances buoyancy.

To this end, it is helpful to consider a scaling analysis of governing equation (1) in the $\hat{\boldsymbol{z}}$ direction. Starting with the force balance of the aggregate, equation (1c), we neglect body forces that are of order $\phi$ and pressure gradients arising from corner flow, which are small at these distances and at small shear viscosity (Spiegelman & McKenzie, 1987). This gives us $P \sim \zeta_\phi \nabla \cdot \boldsymbol{v}_s$, where we have inferred that because the porosity is small, $\zeta_\phi \gg \eta$. Then, taking $(1 - \phi) \sim 1$, expanding conservation of mass equation (1b) at steady state, and using it to eliminate $\nabla \cdot \boldsymbol{v}_s$, we find that
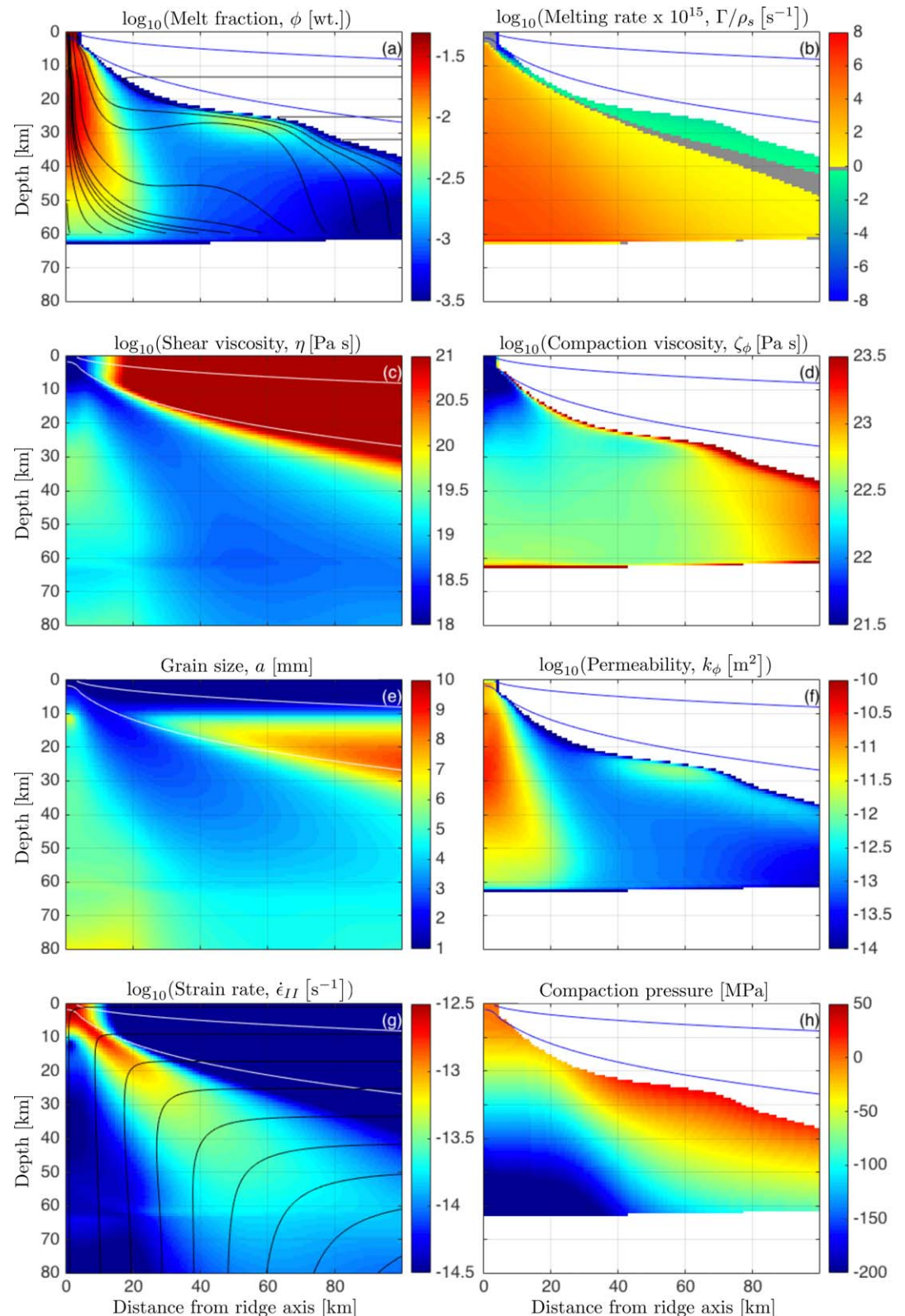
**Figure 2.** The full model run to a steady state. The viscosity is non-Newtonian (equation (2)) with $n = 3.5$ and $m = 2$. Plots and isotherms as in Figure 1. The red lines are contours of the vertical component of the liquid velocity $\boldsymbol{v}_\ell \cdot \hat{\boldsymbol{z}}$. In particular, the dashed contour represents $(\boldsymbol{v}_\ell - \boldsymbol{v}_s) \cdot \hat{\boldsymbol{z}} = 0$ and the solid contour represents $(\boldsymbol{v}_\ell + \boldsymbol{v}_s) \cdot \hat{\boldsymbol{z}} = 0$. Within the region defined by the latter, melt flow is downward.

$$P \sim -\zeta_\phi (\Gamma/\rho - \boldsymbol{v}_s \cdot \nabla \phi). \tag{5}$$

This states that dynamic pressure is associated with the compaction needed to balance melting and maintain constant porosity.

Substituting (5) into Darcy's law (equation (1d)) and rearranging gives $-\boldsymbol{q}/K_\phi \sim \nabla \left[ \zeta_\phi (\boldsymbol{v}_s \cdot \nabla \phi - \Gamma/\rho) \right] + \Delta \rho \boldsymbol{g}$. The case we are interested in is of downward segregation flux $\boldsymbol{q} \cdot \hat{\boldsymbol{z}} \leq 0$ and hence, we consider the vertical balance $\Delta \rho g \lesssim \frac{d}{dz} \left[ \zeta_\phi (\boldsymbol{v}_s \cdot \nabla \phi - \Gamma/\rho) \right]$. The first term on the right-hand side represents advection of porosity by the solid flow. This flow is dominantly upward beneath the lithosphere in the region of interest. Moreover, because melt extraction is efficient, the vertical advection of porosity is much smaller than the production of melt (e.g., Ribe, 1985). Hence, within the zone of negative melt segregation ($\boldsymbol{q} \cdot \hat{\boldsymbol{z}} \leq 0$), it must be the case that

$$\Delta \rho g \lesssim -\frac{1}{\rho} \frac{d}{dz} \zeta_\phi \Gamma. \tag{6}$$

Term-by-term evaluation of the numerical solution for the full model confirms that this approximate balance holds.

It is evident from this analysis that changes in permeability cannot balance the buoyancy of the magma. The permeability (in terms of mobility, $K_\phi$) modulates the segregation flux but, because permeability is scalar and strictly positive, it cannot explain the downward segregation of magma. When the porosity is in steady state, compaction must be in approximate balance with melting ($\nabla \cdot \boldsymbol{v}_s \sim -\Gamma/\rho$); this means that the dynamic pressure scales as $P \sim -\zeta_\phi \Gamma/\rho$. This pressure is typically referred to as the *compaction pressure* and its gradient can drive magmatic segregation. Equation (6) shows that compaction pressure gradients, arising from melting-rate variations, can drive segregation downward, against buoyancy. But the melting-rate field, shown for each of the end-member models in plot (b) of Figures 1 and 2, is nearly identical. Therefore, the melting rate by itself cannot explain the difference in segregation between these two models.

The covariation of melting rate and compaction viscosity $\zeta_\phi$ can explain the emergence of lateral melt transport in the full model. $\zeta_\phi$ is the viscous resistance to compaction and is shown in plot (d) of Figures 1 and 2. In the base model, $\zeta_\phi$ increases upward where $\Gamma$ decreases upward, leading to a product $\zeta_\phi \Gamma$ that is roughly constant. In the full model, both $\zeta_\phi$ and $\Gamma$ decrease upward. The product $\zeta_\phi \Gamma$ is thus not constant; instead has a vertical gradient that is sufficiently negative that the inequality (6) is satisfied.

Hence, the crucial distinction between the base model and the full model is not the grain-size control on melt mobility $K_\phi$, as was hypothesized by Turner et al. (2015). Rather it is the variation in compaction viscosity $\zeta_\phi$ through its dependence on grain size and strain rate, which it inherits from the shear viscosity $\eta$. The grain size itself is sensitive to the strain rate; indeed the rate of grain-size reduction scales with the square of the strain rate (equation (4)). This raises the question of whether the strain rate field, through its influence on viscosity and grain size, can explain melt focusing in the full model. Various studies have shown that if there is an instantaneous balance of the rates of grain growth and reduction on the right-hand side of equation (4), then the mean grain size is given by a power law of the strain rate (Barr & McKinnon, 2007; Rozel et al., 2011; Rudge & Bercovici, 2015). This can be substituted into equation (2) for shear viscosity, and hence, the grain-size dependence can be combined with the strain rate dependence into a single power law with an exponent $n_e = [n(p+1)+m]/(p-m+1)$. Note that while this equation maps $m$, $n$, $p$, to $n_e$, it has no unique inverse; a value of $n_e$ can represent different combinations of primary parameters. We will refer to $n_e$ as the *effective* stress exponent.

Taking empirical values for the stress exponent $n$, grain rheology exponent $m$, and grain growth exponent $p$ (Table 2), the effective stress exponents for pure olivine dislocation and grain-boundary sliding are calculated to be 3.5 and 8, respectively. A similar analysis was used by Hansen et al. (2012) to obtain an empirical flow law for deformation in the grain-boundary sliding regime. They obtained an effective stress exponent of $n_e \sim 4$. In the full model above (Figure 2), where choices of $m$ and $n$ do not correspond to a single deformation mechanism but rather to a balanced state of subequal mechanisms and $p$ is chosen to approximate the effects of grain-size pinning, $n_e = 5.75$. Beyond the question of the active deformation mechanism(s), these differences in $n_e$ arise from uncertainties in the grain growth exponent $p$ and grain rheology exponent $m$. Hence, it is appropriate to consider the dynamics across a range of values of the effective stress dependence (e.g., Rudge & Bercovici, 2015).

**Table 2**
*Parameters m, n, p, and Their Associated Value of the Effective Stress Exponent $n_e$*

| Mechanism | $m$ | $n$ | $p$ | $n_e$ |
|---|---|---|---|---|
| Dislocation | 0 | 3.5 | 3 | 3.5 |
| GBS | 2 | 3.5 | 3 | 8 |
| Full model (Figure 2) | 2 | 3.5 | 5 | 5.75 |
| Unpinned | 2 | 3.5 | 3 | 8 |

*Note.* Isolated deformation mechanisms of pure olivine (parameters from Karato (1989) and Hirth and Kohlstedt (2003)) are given in the top two rows; the bottom rows represent the case of a balance of mechanisms (De Bresser et al., 1998, 2000). Diffusion creep is excluded from the table because in isolation it does not cause grain-size reduction. If diffusion creep makes a significant contribution to the deformation rate it will modify $n_e$.

Figure 3 shows output from simulations with different values of the effective stress exponent, run to steady state (using $n = n_e$ in equation (2) for the shear viscosity). The grain size is constant and uniform in these models. This ensures that the permeability is not affected by grain-size variation; however, the rheological consequences of grain-size variation are captured indirectly, through the use of $n_e$. The top row of plots has $n_e = 1$, making it identical to the base model shown in Figure 1. Subsequent rows have $n_e = 2$, 3.5, 5.75, and 8. These values for $n_e$ are based on experimental constraints on the viscosity parameters $n$, $m$ and the grain growth exponent $p$ for the dominant deformation mechanisms in olivine. Hence, while $n_e$ directly controls the variation of shear viscosity with stress (or strain rate), it also represents the sensitivity of viscosity to the dynamics of mean grain size.

The shear viscosity field is shown in the second column of Figure 3. With increasing $n_e$, a low-viscosity layer dipping at about 45° emerges. The position of this layer is set by the kinematic structure of corner flow; namely, where the solid turns from upwelling to lateral motion there is a larger strain rate that reduces the viscosity. This variation in $\eta$ is mirrored in the compaction viscosity. Note that while the effective stress exponent $n_e$ is formally related to the grain-size dynamics (parameters $p$, $m$) and the inherent stress dependence of viscosity (parameter $n$), the calculations shown in Figure 3 are independent of the parameters used to compute $n_e$.

The first column in Figure 3 shows porosity and magma streamlines for increasing values of $n_e$. For larger effective stress exponents, viscosity variations give rise to compaction pressure gradients (equation (6)) that focus melt. The pattern of melt transport looks increasingly similar to the pattern in the full model of Figure 2, even resulting in a region of downward melt segregation. This demonstrates that the difference between the full model and the base model is a consequence of the strain rate control (or, equivalently, the stress control) on viscosity and not the influence of grain size on permeability.

This finding is interesting, in part, because it is in stark contrast to the invariance of the solid flow under changes to the effective stress exponent. This invariance is evident in the comparison of the melting-rate field in plot (b) of Figures 1 and 2, which reflects the solid upwelling rate. The solid flow is tightly constrained by the kinematic boundary conditions and the thermally imposed structure of the lithosphere. The liquid flow, however, is free to respond to pressure gradients arising from the dynamics and, in this case, from the compaction pressure associated with melt extraction. The connection between melting, compaction viscosity, and compaction pressure that was highlighted in the scaling analysis, above, is the crucial link between rheology and melt extraction.

## 5. Discussion and Conclusion

The results presented above represent a previously unexamined form of magmatic focusing at mid-ocean ridges. This mechanism does not rely on the dynamic pressure gradient associated with corner flow (Spiegelman & McKenzie, 1987) or melt transport along a sublithospheric channel (Sparks & Parmentier, 1991), though both of these mechanisms can and do play a minor role in the full model shown in Figure 2. Instead, this focusing mechanism relies on gradients in compaction pressure that arise from variations in viscosity and melting rate. These variations are, in turn, controlled by the characteristic corner flow structure of mantle deformation beneath mid-ocean ridges. To zeroth order, this flow structure is determined by the boundary conditions associated with plate separation and is insensitive to viscosity variations. Specifically, corner flow leads to a triangular region of upwelling with its apex at the mid-ocean ridge axis. This upwelling controls the melting-rate field $\Gamma$. The transition from upwelling to horizontal flow occurs along the sides of the triangle, which slope downward away from the ridge axis at an angle of ~45°. The enhanced strain rate associated with this transition controls both the variation in grain size $a$ and non-Newtonian viscosity $\eta$ (and $\zeta_\phi$).

In the full model, the melting rate increases toward the ridge axis, while the bulk viscosity remains roughly constant. This results in a spatial structure of $\zeta_\phi\Gamma$ that drives melt flow laterally from the flanks of the melting region toward the ridge. This can be understood by considering the balance of compaction and melting when the melt fraction is constant. At this steady state, melt must segregate as fast as it is produced
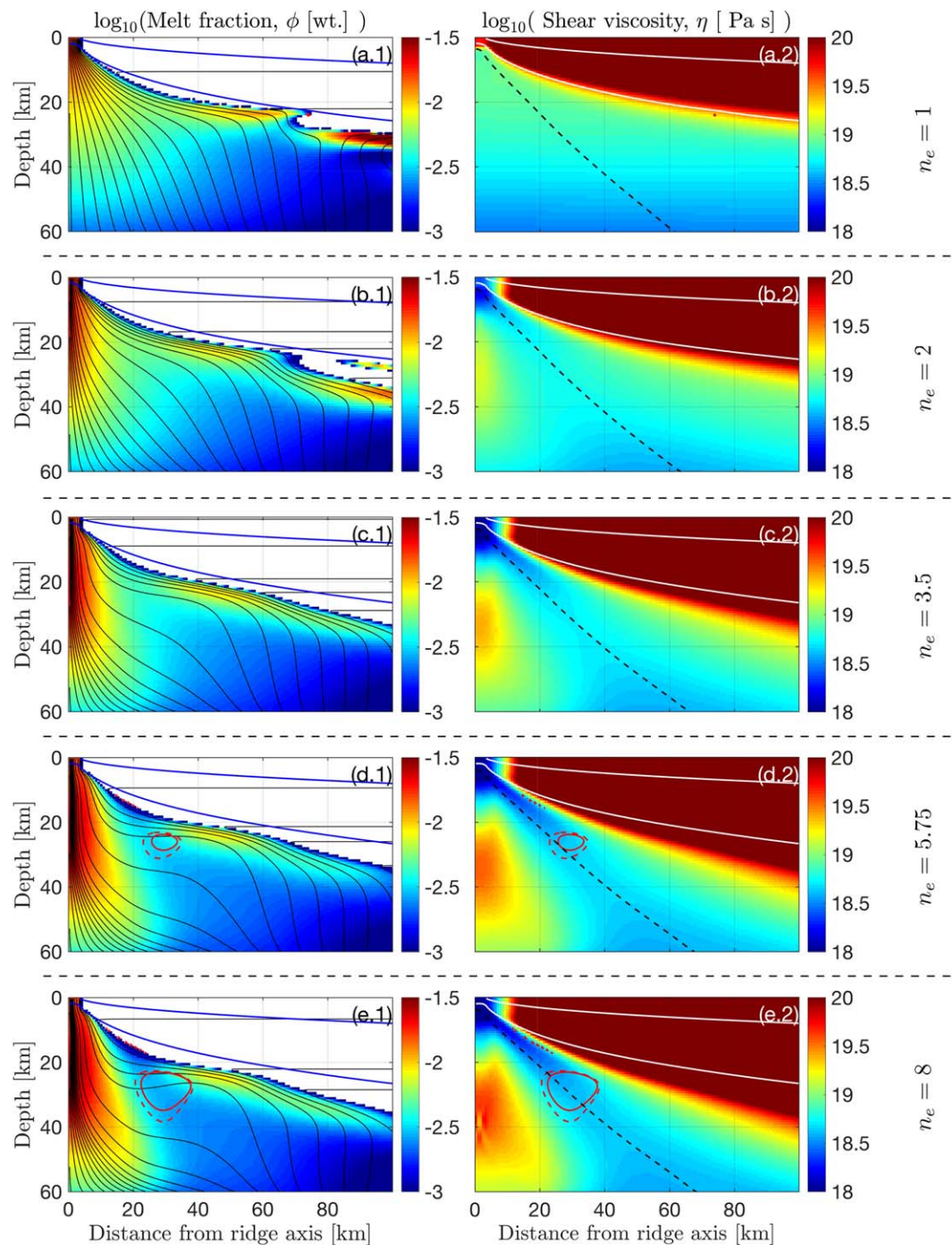
**Figure 3.** Model sensitivity to the effective stress exponent $n_e$. The first column shows the base-10 logarithm of melt fraction with streamlines of magma velocity $\boldsymbol{v}_\ell$ superimposed. The second column shows the base-10 logarithm of shear viscosity $\eta$. Rows show simulation output at steady state for $n_e = 1$, 2, 3.5, 5.75, and 8. Isotherms at 600°C and 1,250°C are shown in all plots with blue or white lines. The red lines are contours as described in the caption of Figure 2. The black dashed line connects points where $\boldsymbol{v}_s \cdot (\hat{\boldsymbol{x}} - \hat{\boldsymbol{z}}) = 0$; i.e., where the solid corner flow transitions from upwelling to lateral flow. Note that in these models, normalized grain size $\langle a \rangle = 1$ (equation (2)) and hence $m$ is irrelevant. The grain growth exponent $p = 5$ is constant.

(neglecting the advection of melt fraction, which is small). In other words, the solid phase must converge at a rate that is given by the volume production rate of magma, $-\nabla \cdot \boldsymbol{v}_s \sim \Gamma / \rho$. A convergent solid flow means the magma is underpressured, i.e., that the compaction pressure is negative. This underpressure

increases in magnitude with the compaction viscosity. Hence, regions with slower melting rates and/or lower viscosities have larger (less negative) compaction pressure. The resulting compaction pressure gradient drives melt toward regions of larger $\zeta_\phi \Gamma$.

The compaction pressure gradient associated with $\zeta_\phi \Gamma$ in the full model is enhanced by the focusing process itself. Focusing concentrates melt into a column of mantle directly beneath the ridge axis. The larger melt fractions in this column produce a high-permeability connection between the surface and the melting region below. High permeability promotes a larger compaction length, and hence, the transmission of low compaction pressure from the ridge axis to depth.

Figure 4 is a schematic illustration of our hypothesized focusing mechanism (right) compared to the sublithospheric decompaction-channel mechanism of Sparks and Parmentier (1991) (left). The resistivity field obtained by Key et al. (2013) is shown in the background. Focusing associated with a sublithospheric channel predicts a distribution of melt fraction that is inconsistent with that implied by the resistivity data. In particular, the rapid, vertical extraction of melt below the decompaction channel should result in higher and more uniform resistivity throughout the melting region. Thus this model cannot explain the steep-sided shape of the low-resistivity region beneath the axis. By contrast, the full model predicts magma to move laterally at depths above the onset of silicate melting and concentrate beneath the ridge axis (Figure 4). This melt distribution is more consistent, qualitatively, with the MT inversion, which shows a minimum in resistivity directly beneath the ridge axis.

The pattern of melt flow obtained in the present study differs from that of Keller et al. (2017). This is due to the assumptions of constant grain size and Newtonian viscosity by Keller et al. (2017)—a conservative approach to modeling the rheology, in line with previous studies. The present study deviates from foregoing work by investigating a non-Newtonian viscosity that could arise when grain size is controlled by the instantaneous balance of growth and recrystallization. A further difference stems from Keller et al. (2017)'s incorporation of volatile elements and their effect on melting and melt transport. Results of those models suggest that volatiles promote deep, reactive channelization of magmatic flux (see also Keller & Katz, 2016). Volatiles are neglected from the models presented here. Moreover, our current understanding is insufficient for any speculation on how volatiles and channelized melt transport might interact with the non-Newtonian dynamics.

The focusing mechanism we propose is different in many of its details from that suggested by Turner et al. (2015). Their hypothesis was based on the permeability structure arising from variations in mean grain size. The grain-size variations obtained in the full model above (Figure 2) are largely consistent with Turner et al. (2015). However, our numerical experiments using constant grain size and large $n_e$ in section 4 show that
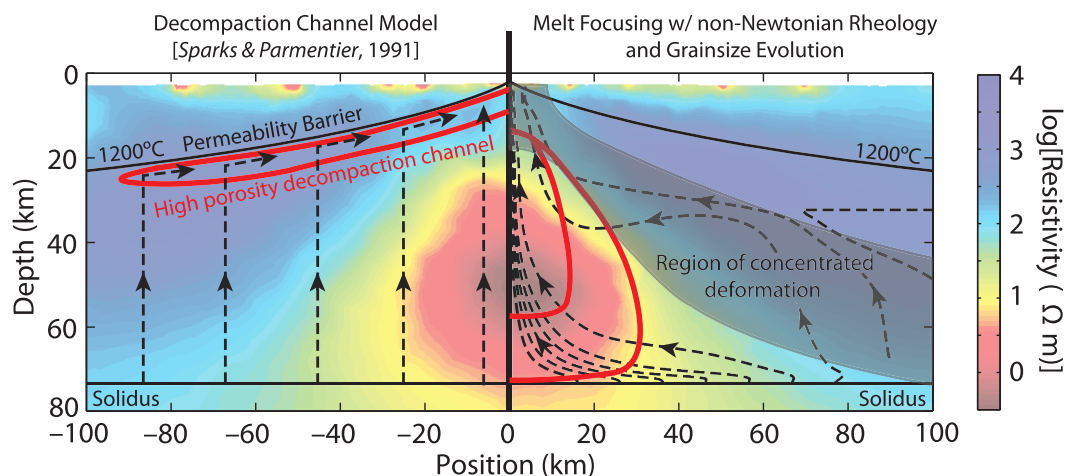


**Figure 4.** Schematic diagram of two hypotheses for melt focusing. The background image is the resistivity structure of the northern East Pacific Rise at 9°30′N as obtained by Key et al. (2013). The magma streamlines on the left side of the diagram represent the focusing hypothesis of Sparks and Parmentier (1991). Streamlines on the right side of the diagram are derived from the full model (Figure 2) and depict the hypothesis proposed here. Red curves on both sides outline the region of increased melt fraction.

focusing is not a direct consequence of the permeability structure. Furthermore, the scaling analysis presented above supports the idea that viscosity and melting-rate variations are most important in promoting melt focusing. Thus, while grain size can be important in influencing mantle viscosity, its effect on mantle permeability does not exert a significant control on melt focusing.

This conclusion raises a more general point regarding two-phase models of coupled magma/mantle flow. For convenience and simplicity, those models have generally neglected the non-Newtonian stress dependence that arises from dislocation-based creep mechanisms and/or grain-size dynamics when computing two-phase flow (e.g., Katz, 2010; Keller et al., 2017). This has been justified on the grounds that the kinematically driven mantle flow field is little affected by this exclusion. However, the results presented here suggest that despite the invariance of the solid flow, the pattern of magmatic segregation is very sensitive to the stress dependence of mantle viscosity. Although this has been noted in models of laboratory-scale two-phase flow (Katz et al., 2006), it was unrecognized in the context of larger-scale tectonic models. Future work should more thoroughly explore the consequences of non-Newtonian viscosity for melt segregation in different geologic environments.

## References

Amestoy, P. R., Duff, I. S., Koster, J., & L'excellent, J.-Y. (2001). A fully asynchronous multifrontal solver using distributed dynamic scheduling. *SIAM Journal on Matrix Analysis and Applications*, *23*(1), 15–41.

Atkinson, H. (1988). Overview no. 65: Theories of normal grain growth in pure single phase systems. *Acta Metallurgica*, *36*, 469–491.

Austin, N., & Evans, B. (2009). The kinetics of microstructural evolution during deformation of calcite. *Journal of Geophysical Research*, *114*, B09402. https://doi.org/10.1029/2008JB006138

Austin, N. J., & Evans, B. (2007). Paleowattmeters: A scaling relation for dynamically recrystallized grain size. *Geology*, *35*(4), 343–346.

Bai, H., & Montési, L. (2015). Slip-rate-dependent melt extraction at oceanic transform faults. *Geochemistry, Geophysics, Geosystems*, *16*, 401–419. https://doi.org/10.1002/2014GC005579

Balay, S., Abhyankar, S., Adams, M. F., Brown, J., Brune, P., Buschelman, K.,. . . Zhang, H. (2016a). *PETSc Web page*. Lemont, IL: Argonne National Laboratory. Retrieved from http://www.mcs.anl.gov/petsc

Balay, S., Abhyankar, S., Adams, M. F., Brown, J., Brune, P., Buschelman, K.,. . . Zhang, H. (2016b). *PETSc users manual* (Tech. Rep. ANL-95/11-Revision 3.7). Lemont, IL: Argonne National Laboratory. Retrieved from http://www.mcs.anl.gov/petsc

Barr, A. C., & McKinnon, W. B. (2007). Convection in ice I shells and mantles with self-consistent grain size. *Journal of Geophysical Research*, *112*, E02012. https://doi.org/10.1029/2006JE002781

Behn, M. D., Hirth, G., & Elsenbeck, J. R. (2009). Implications of grain size evolution on the seismic structure of the oceanic upper mantle. *Earth and Planetary Science Letters*, *282*(1–4), 178–189

Burke, J., & Turnbull, D. (1952). Recrystallization and grain growth. *Progress in Metal Physics*, *3*, 220–292.

Cagnioncle, A.-M., Parmentier, E., & Elkins-Tanton, L. (2007). Effect of solid flow above a subducting slab on water distribution and melting at convergent plate boundaries. *Journal of Geophysical Research*, *112*, B09402. https://doi.org/10.1029/2007JB004934

Carbotte, S. M., Smith, D. K., Cannat, M., & Klein, E. (2015). Tectonic and magmatic segmentation of the Global Ocean Ridge System: A synthesis of observations. *Geological Society Special Publications*, *420*, 1–47. https://doi.org/10.1144/SP420.5

Cerpa, N. G., Wada, I., & Wilson, C. R. (2017). Fluid migration in the mantle wedge: Influence of mineral grain size and mantle compaction. *Journal of Geophysical Research*, *122*, 6247–6268. https://doi.org/10.1002/2017JB014046

De Bresser, J., Ter Heege, J., & Spiers, C. (2000). Grain size reduction by dynamic recrystallization: Can it result in major rheological weakening? *International Journal of Earth Sciences*, *90*(1), 28–45.

De Bresser, J. H. P., Peach, C. J., Reijs, J. P. J., & Spiers, C. J. (1998). On dynamic recrystallization during solid state flow: Effects of stress and temperature. *Geophysical Research Letters*, *25*(18), 3457–3460.

Forsyth, D. W., Scheirer, D., Webb, S. C., Dorman, L., Orcutt, J., Harding, A.,. . . Wilcock, W. S. D. (1998). Imaging the deep seismic structure beneath a mid-ocean ridge: The MELT experiment. *Science*, *280*, 1215–1218.

Ghods, A., & Arkani-Hamed, J. (2000). Melt migration beneath mid-ocean ridges. *Geophysical Journal International*, *140*(3), 687–697. https://doi.org/10.1046/j.1365-246X.2000.00032.x

Gregg, P. M., Behn, M. D., & Grove, T. L. (2009). Melt generation, crystallization, and extraction beneath segmented oceanic transform faults. *Journal of Geophysical Research*, *114*, B11102. https://doi.org/10.1029/2008JB006100

Hansen, L. N., & Warren, J. M. (2015). Quantifying the effect of pyroxene on deformation of peridotite in a natural shear zone. *Journal of Geophysical Research: Solid Earth*, *120*, 2717–2738. https://doi.org/10.1002/2014JB011584

Hansen, L. N., Zimmerman, M. E., & Kohlstedt, D. L. (2012). The influence of microstructure on deformation of olivine in the grain-boundary sliding regime. *Journal of Geophysical Research*, *117*, B09201. https://doi.org/10.1029/2012JB009305

Hebert, L. B., & Montési, L. G. J. (2010). Generation of permeability barriers during melt extraction at mid-ocean ridges. *Geochemistry, Geophysics, Geosystems*, *11*, Q12008. https://doi.org/10.1029/2010GC003270

Hillert, M. (1965). On the theory of normal and abnormal grain growth. *Acta Metallurgica*, *13*, 227–238.

Hiraga, T., Tachibana, C., Ohashi, N., & Sano, S. (2010). Grain growth systematics for forsterite $\pm$enstatite aggregates: Effect of lithology on grain size in the upper mantle. *Earth and Planetary Science Letters*, *291*(1), 10–20.

Hirth, G., & Kohlstedt, D. (2003). Rheology of the upper mantle and the mantle wedge: A view from the experimentalists. In J. Eiler (Ed.), *Inside the subduction factory* (pp. 83–105). Washington, DC: American Geophysical Union.

Hirth, G., & Kohlstedt, D. L. (1995). Experimental constraints on the dynamics of the partially molten upper-mantle. 2. Deformation in the dislocation creep regime. *Journal of Geophysical Research*, *100*, 15441–15449.

Karato, S.-I. (1989). Grain growth kinetics in olivine aggregates. *Tectonophysics*, *168*, 255–273.

Katz, R. (2008). Magma dynamics with the enthalpy method: Benchmark solutions and magmatic focusing at mid-ocean ridges. *Journal of Petrology*, *49*(12), 2099–2121. https://doi.org/10.1093/petrology/egn058

Katz, R., Knepley, M., Smith, B., Spiegelman, M., & Coon, E. (2007). Numerical simulation of geodynamic processes with the Portable Extensible Toolkit for Scientific Computation. *Physics of the Earth and Planetary Interiors*, *163*, 52–68. https://doi.org/10.1016/j.pepi.2007.04.016

Katz, R. F. (2010). Porosity-driven convection and asymmetry beneath mid-ocean ridges. *Geochemistry, Geophysics, Geosystems*, *11*, Q0AC07. https://doi.org/10.1029/2010GC003282

Katz, R. F., Spiegelman, M., & Holtzman, B. (2006). The dynamics of melt and shear localization in partially molten aggregates. *Nature*, *442*, 676–679. https://doi.org/10.1038/nature05039

Kelemen, P., Hirth, G., Shimizu, N., Spiegelman, M., & Dick, H. (1997). A review of melt migration processes in the adiabatically upwelling mantle beneath oceanic spreading ridges. *Philosophical Transactions of the Royal Society of London Series A*, *355*, 283–318.

Keller, T., & Katz, R. (2016). The role of volatiles in reactive melt transport in the asthenosphere. *Journal of Petrology*, *57*(6), 1073–1108. https://doi.org/10.1093/petrology/egw030

Keller, T., Katz, R., & Hirschmann, M. M. (2017). Volatiles beneath mid-ocean ridges: Deep melting, channelised transport, focusing, and metasomatism. *Earth and Planetary Science Letters*, *464*, 55–68. https://doi.org/10.1016/j.epsl.2017.02.006

Key, K., Constable, S., Liu, L., & Pommier, A. (2013). Electrical image of passive mantle upwelling beneath the northern East Pacific Rise. *Nature*, *495*, 499–502.

Magde, L. S., & Sparks, D. W. (1997). Three-dimensional mantle upwelling, melt generation, and melt migration beneath segment slow spreading ridges. *Journal of Geophysical Research*, *102*, 20571–20583.

McKenzie, D. (1984). The generation and compaction of partially molten rock. *Journal of Petrology*, *25*(3), 713–765. https://doi.org/10.1093/petrology/25.3.713

Miller, K. J., Montési, L. G., & Zhu, W. (2015). Estimates of olivine-basaltic melt electrical conductivity using a digital rock physics approach. *Earth and Planetary Science Letters*, *432*, 332–341. https://doi.org/10.1016/j.epsl.2015.10.004

Miller, K. J., Zhu, W., Montési, L. G., & Gaetani, G. A. (2014). Experimental quantification of permeability of partially molten mantle rock. *Earth and Planetary Science Letters*, *388*, 273–282. https://doi.org/10.1016/j.epsl.2013.12.003

Montési, L. G. J., Behn, M. D., Hebert, L. B., Lin, J., & Barry, J. L. (2011). Controls on melt migration and extraction at the ultraslow southwest Indian ridge 10°–16°E. *Journal of Geophysical Research*, *116*, B10102. https://doi.org/10.1029/2011JB008259

Nichols, S. J., & Mackwell, S. J. (1991). Grain growth in porous olivine aggregates. *Physics and Chemistry of Minerals*, *18*(4), 269–278.

Phipps Morgan, J. (1987). Melt migration beneath mid-ocean spreading centers. *Geophysical Research Letters*, *14*(12), 1238–1241.

Ribe, N. M. (1985). The deformation and compaction of partial molten zones. *Geophysical Journal International*, *83*(2), 487–501. https://doi.org/10.1111/j.1365-246X.1985.tb06499.x

Rozel, A., Ricard, Y., & Bercovici, D. (2011). A thermodynamically self-consistent damage equation for grain size evolution during dynamic recrystallization. *Geophysical Journal International*, *184*(2), 719–728. https://doi.org/10.1111/j.1365-246X.2010.04875.x

Rudge, J. F. (2014). Analytical solutions of compacting flow past a sphere. *Journal of Fluid Mechanics*, *746*, 466–497. https://doi.org/10.1017/jfm.2014.109

Rudge, J. F., & Bercovici, D. (2015). Melt-band instabilities with two-phase damage. *Geophysical Journal International*, *201*, 640–651. https://doi.org/10.1093/gji/ggv040

Scott, D. R., & Stevenson, D. J. (1986). Magma ascent by porous flow. *Journal of Geophysical Research*, *91*, 9283–9296.

Shorttle, O., Maclennan, J., & Lambart, S. (2014). Quantifying lithological variability in the mantle. *Earth and Planetary Science Letters*, *395*, 24–40.

Simpson, G., Spiegelman, M. W., & Weinstein, M. (2010a). A multiscale model of partial melts: 1. Effective equations. *Journal of Geophysical Research*, *115*, B04410. https://doi.org/10.1029/2009JB006375

Simpson, G., Spiegelman, M. W., & Weinstein, M. (2010b). A multiscale model of partial melts: 2. Numerical results. *Journal of Geophysical Research*, *115*, B04411. https://doi.org/10.1029/2009JB006376

Sparks, D. W., & Parmentier, E. (1991). Melt extraction from the mantle beneath spreading centers. *Earth and Planetary Science Letters*, *105*(4), 368–377. https://doi.org/10.1016/0012-821X(91)90178-K

Spiegelman, M., & McKenzie, D. (1987). Simple 2-d models for melt extraction at mid-ocean ridges and island arcs. *Earth and Planetary Science Letters*, *83*(1–4), 137–152. https://doi.org/10.1016/0012-821X(87)90057-4

Spiegelman, M. W. (1993a). Flow in deformable porous-media. 2. Numerical-analysis—The relationship between shock-waves and solitary waves. *Journal of Fluid Mechanics*, *247*, 39–63.

Spiegelman, M. W. (1993b). Physics of melt extraction—Theory, implications and applications. *Philosophical Transactions of the Royal Society of London Series A*, *342*, 23–41.

Takei, Y., & Holtzman, B. K. (2009). Viscous constitutive relations of solid-liquid composites in terms of grain boundary contiguity: 2. Compositional model for small melt fractions. *Journal of Geophysical Research*, *114*, B06206. https://doi.org/10.1029/2008JB005851

Tasaka, M., & Hiraga, T. (2013). Influence of mineral fraction on the rheological properties of forsterite + enstatite during grain-size-sensitive creep: 1. Grain size and grain growth laws. *Journal of Geophysical Research: Solid Earth*, *118*, 3970–3990. https://doi.org/10.1002/jgrb.50285

Tasaka, M., Hiraga, T., & Michibayashi, K. (2014). Influence of mineral fraction on the rheological properties of forsterite + enstatite during grain size sensitive creep: 3. Application of grain growth and flow laws on peridotite ultramylonite. *Journal of Geophysical Research: Solid Earth*, *119*, 840–857. https://doi.org/10.1002/2013JB010619

Tasaka, M., Hiraga, T., & Zimmerman, M. E. (2013). Influence of mineral fraction on the rheological properties of forsterite + enstatite during grain-size-sensitive creep: 2. Deformation experiments. *Journal of Geophysical Research: Solid Earth*, *118*, 3991–4012. https://doi.org/10.1002/jgrb.50284

Thielmann, M., Rozel, A., Kaus, B. J. P., & Ricard, Y. (2015). Intermediate-depth earthquake generation and shear zone formation caused by grain size reduction and shear heating. *Geology*, *43*, 791–794. https://doi.org/10.1130/G36864.1

Turner, A. J., Katz, R. F., & Behn, M. D. (2015). Grain-size dynamics beneath mid-ocean ridges: Implications for permeability and melt extraction. *Geochemistry, Geophysics, Geosystems*, *16*, 925–946. https://doi.org/10.1002/2014GC005692

von Bargen, N., & Waff, H. S. (1986). Permeabilities, interfacial areas and curvatures of partially molten systems: Results of numerical computations of equilibrium microstructures. *Journal of Geophysical Research*, *91*, 9261–9276.

Wada, I., & Behn, M. D. (2015). Focusing of upward fluid migration beneath volcanic arcs: Effect of mineral grain size variation in the mantle wedge. *Geochemistry, Geophysics, Geosystems*, *16*, 3905–3923. https://doi.org/10.1002/2015GC005950

Wada, I., Behn, M. D., & He, J. (2011). Grain-size distribution in the mantle wedge of subduction zones. *Journal of Geophysical Research*, *116*, B10203. https://doi.org/10.1029/2011JB008294

White, R. S., Minshull, T. A., Bickle, M. J., & Robinson, C. J. (2001). Melt generation at very slow-spreading oceanic ridges: Constraints from geochemical and geophysical data. *Journal of Petrology*, *42*, 1171–1196.